



Research articles

Effects of size and anisotropy of magnetic nanoparticles associated with dynamics of easy axis for magnetic particle imaging



Satoshi Ota^{a,*}, Yuki Matsugi^b, Takeru Nakamura^b, Ryoji Takeda^c, Yasushi Takemura^c,
Ichiro Kato^d, Satoshi Nohara^d, Teruyoshi Sasayama^b, Takashi Yoshida^b, Keiji Enpuku^b

^a Department of Electrical and Electronic Engineering, Shizuoka University, Hamamatsu 432-8561, Japan

^b Department of Electrical Engineering, Kyushu University, Fukuoka 819-0385, Japan

^c Department of Electrical and Computer Engineering, Yokohama National University, Yokohama 240-8501, Japan

^d The Nagoya Research Laboratory, Meito Sangyo Co. Ltd., Kiyosu 452-0067, Japan

ARTICLE INFO

Keywords:

Magnetic nanoparticles
Magnetic particle imaging
Particle structure
Anisotropy
Core size distribution
Easy axis

ABSTRACT

The structure of magnetic nanoparticles affects the signal intensity and resolution of magnetic particle imaging, which is derived from the harmonics caused by the nonlinear response of magnetization. To understand the key effects of particle structures on the magnetization harmonics, the dependence of the harmonics on the size and anisotropy of different structures was investigated. We measured the harmonic signals with respect to different magnetic nanoparticle structures by applying an AC field with a gradient field for magnetic particle imaging, which was compared with the numerically simulated magnetization properties. In addition, the dynamics of the easy axis of magnetic nanoparticles in the liquid state were evaluated. The difference between the harmonics in the solid and liquid states indicates the effective core size and anisotropy due to particle structures such as single-core, chainlike, and multicore particles. In the case of the chainlike structure, the difference between the harmonics in the solid and liquid states was larger than other structures. In the numerical simulations, core diameters and anisotropy constants were considered as the effective values, such as the increase in anisotropy in the chainlike structure due to dipole interaction. The multicore particles showed high harmonics owing to their large effective core diameters. The superparamagnetic regime in the multicore structure despite the large effective core diameter was derived from the small effective anisotropy. The effective core size and the effective anisotropy of each particle structure and their impacts on the harmonic signals were revealed.

1. Introduction

Magnetic particle imaging (MPI) was developed as an imaging method for magnetic nanoparticles (MNPs) [1]. The traceability of MPI with respect to the MNPs in blood was investigated with the time evolution of the location of MNPs in an animal model [2,3]. Cancer detection through MPI was conducted by using MNPs functionalized with materials conjugating with cancer cells, such as lactoferrin, which is a peptide, to target brain cancer [4,5]. Monitoring the transplantation of magnetically functionalized stem cells using MPI was examined to promote the efficacy of stem cell therapy, such as the regeneration of cardiac tissue [6,7]. Islet transplantation was successfully conducted by labeling pancreatic islets using MNPs for MPI monitoring [8].

MNPs with large-amplitude harmonics were investigated to advance MPI. Harmonic amplitude is influenced by the size and structure of MNPs [9]. In general, MNPs with a large core diameter exhibited

nonlinear response to an applied field of low flux density, which induced the large-amplitude harmonics [10,11]. It was also been found that the core diameter of 24.4 nm showed the clearest image in the core diameters from 18.5 nm to 32.1 nm with low anisotropy [12]. With regard to the structural effect, the multicore structure provided the large-amplitude harmonics [13]. Multicore particles are composed of a large effective core as the aggregated single-core particles [14]. The magnetization behavior of the multicore structure is influenced not by each single-core diameter, but by the effective cluster diameter [15].

The difference between the harmonic amplitude in the solid and liquid states indicates that the MNPs fixed in a tumor are distinguished from the MNPs dispersed in blood in the human body with respect to MPI signals [9]. Only magnetization is rotated without changing the spatial rotation of the particle volume in the solid state, which is observed as Néel relaxation. On the contrary, the easy axes rotate in addition to magnetization in the liquid state as Brownian relaxation. The

* Corresponding author.

E-mail address: ota.s@shizuoka.ac.jp (S. Ota).

<https://doi.org/10.1016/j.jmmm.2018.11.043>

Received 23 June 2018; Received in revised form 24 September 2018; Accepted 6 November 2018

Available online 07 November 2018

0304-8853/ © 2018 Elsevier B.V. All rights reserved.

viscosity of the medium associated with Brownian relaxation time significantly affects the magnetization dynamics through the change in the dynamics of the easy axis [16–18]. We clearly observed easy-axis rotation with time delay from magnetization rotation by applying pulse fields as a transition response [19]. The influence of particle core diameters associated with the anisotropy energy on the rotational degree of the easy axis was evaluated. Furthermore, the dynamics of the easy axis of the MNPs dispersed in liquid were numerically and experimentally observed as a static response [16,20].

In this study, MPI signals were measured for blood-pooling MNPs of different sizes and structures. We evaluated the effect of the core size and anisotropy associated with particle structure on the harmonic derived from the nonlinear response of MNPs. Moreover, the influence of the dynamics of the easy axis on the harmonic in the liquid state was assessed.

2. Materials and methods

2.1. Measured MNPs

The following water-based maghemite nanoparticles, which were supplied by Meito Sangyo Co. Ltd., Kiyosu, Japan, were analyzed: CMEADM-004 (sample I), CMEADM-023 (sample II), CMEADM-033 (sample III), and CMEADM-033-02 (sample IV). These MNPs were coated by carboxymethyl-diethylaminoethyl dextran, which is negatively charged and enhances the blood-pooling capability of MNPs [21]. For Samples I, II, III, and IV, the mean core diameters measured with a transmission electronic microscopy (TEM) were 4, 8, 5–6, and 6 nm, the mean hydrodynamic diameters measured by dynamic light scattering were 38, 83, 54, and 64 nm, and the saturation magnetic moments measured by the DC magnetization curves were 98, 113, 104, and 119 A m²/kg-Fe, respectively [9]. The concentration of the analyzed samples was 28 mg-Fe/mL.

2.2. Measurement of 2D MPI and AC magnetic properties

A set of permanent magnets, a set of two drive coils to apply an AC field, and a pick-up coil including a differential coil were prepared to measure the third harmonic magnetization as the signal for 2D MPI. A gradient field was applied to select the field free point (FFP) using the permanent magnets, whose gradient was 1 T/m along the x-axis and 2 T/m along the y-axis. The maximal flux density and frequency of the applied AC field were 3.5 mT and 3 kHz, respectively. The 2D images were constructed by directly plotting the real part of the measured third harmonic in the x-y plane. The position of the FFP and the set of detection coils were fixed. The sample position was moved to scan samples for 2D MPI. The real part of the third harmonic was detected by a lock-in amplifier.

In addition, the magnetization signals of each sample were measured in an AC field with the maximal flux density of 10 mT and frequency of 10 kHz, using a detection circuit that included pick-up and differential coils located in an excitation coil without the gradient field [9]. The signal derived from the applied field was reduced by the differential coil, and was completely canceled out by subtracting the signal detected from the pick-up coil without samples from the signal with samples. To evaluate the nonlinear response of the magnetization to the applied AC field, the third harmonic was analyzed from the measured magnetization signal with the Fourier transform method.

2.3. Numerical simulation

The dynamics of the magnetization with the rotation of the easy axis in the liquid state are calculated using [16,22,23]

$$\frac{d\mathbf{m}}{dt} = \omega \times \mathbf{m} - \frac{\gamma}{1 + \alpha^2} \left[\mathbf{m} \times \left(\mathbf{H}_{\text{eff}} - \frac{\omega}{\gamma} \right) + \alpha \mathbf{m} \times \left\{ \mathbf{m} \times \left(\mathbf{H}_{\text{eff}} - \frac{\omega}{\gamma} \right) \right\} \right], \quad (1)$$

where \mathbf{m} , γ , α , \mathbf{H}_{eff} , and ω are the magnetic moment, gyromagnetic ratio, damping parameter ($\alpha = 0.1$), effective field, and angular velocity of a particle, respectively. Magnetic moment was calculated as the value normalized by saturated magnetic moment M_s in MKSA system of units. The gyromagnetic ratio is estimated as $\gamma = \mu_0 M_s V_M (1 + \alpha^2) / (2\alpha \tau_N k_B T)$, where μ_0 is the permeability of free space, V_M is the volume of a single-domain particle, τ_N is the zero-field Néel relaxation time, k_B is the Boltzmann constant (1.38×10^{-23} J/K), and T is the temperature in Kelvin [24]. The effective field is composed of the excitation field (\mathbf{H}_{ex}), anisotropy field (\mathbf{H}_{an}), and fluctuating field (\mathbf{H}_{th}) due to thermal disturbance to consider the Zeeman, anisotropy, and thermal energies associated with MNPs, respectively. The anisotropy field is estimated as $\mathbf{H}_{\text{an}} = 2K_u(\mathbf{m} \cdot \mathbf{n})\mathbf{n} / (\mu_0 M_s)$, where K_u is the effective anisotropy constant including crystal, surface, and shape effects, and \mathbf{n} is the unit vector of the easy axis. In addition, the angular velocity associated with particle rotation is given by

$$\omega = \frac{1}{\xi} \{ \mu_0 M_s V_M \mathbf{m} \times (\mathbf{H}_{\text{ex}} + \mathbf{H}_{\text{th}}) + \Gamma \}, \quad (2)$$

where ξ and Γ are the friction coefficient and random torque due to thermal fluctuation, respectively. The friction coefficient depends on viscosity η and particle hydrodynamic volume V_H . It is estimated by $\xi = 6\eta V_H$, which is originally applied for spherical particles. In the chainlike structure, the shape anisotropy was increased by the dipole interaction as the shape effect. In this simulation, particularly to evaluate the influences of the effective size and the effective anisotropy of MNPs on the harmonics, the parameters other than the size and anisotropy is not changed. In addition, because a thermal fluctuation field affects the magnetization and the random torque affects the easy axis, these factors are separately defined. The fluctuating field and random torque due to thermal disturbance have Gaussian distributions with zero mean. The variance of the zero mean fluctuating field and random torque due to thermal disturbance satisfied the following equations:

$$\langle H_{th,i}(t) H_{th,j}(t') \rangle = \frac{2\alpha}{1 + \alpha^2} \frac{k_B T}{\gamma \mu_0 M_s V_M} \delta_{ij} \delta(t - t'), \quad (3)$$

$$\langle \Gamma_i(t) \Gamma_j(t') \rangle = 2\xi k_B T \delta_{ij} \delta(t - t'), \quad (4)$$

In Eqs. (3) and (4), i and j are Cartesian indices of different particles. δ_{ij} is the Kronecker delta function, and δ is the Dirac delta function. The orientation of the easy axis is calculated by the differential equation of the unit vector of the easy axis, as follows: $d\mathbf{n}/dt = \omega \times \mathbf{n}$. The differential equations in terms of the numerical simulations were solved with the Runge-Kutta method.

With respect to the model in the solid state, the term including ω was omitted in Eq. (1). In the numerical simulations, 28,672 particles were set. A saturation magnetic moment of 96 A m²/kg-Fe was applied to all particles. In particular, the hydrodynamic particles in the experiment are composed of the aggregated core particles, which is complex matter. To simplify the simulation model, the hydrodynamic diameter was equal to the effective core diameter. The temperature was 300 K, and the viscosity was 0.89 mPa s. The flux density and frequency of the applied field were 10 mT and 10 kHz, respectively.

2.4. Size distribution of MNP in experiments and numerical simulations

Fig. 1(a) shows the volume distributions normalized by the total volume with respect to the core diameter of each sample estimated from DC magnetization curves [25]. The DC magnetization curves were measured in our previous research [9]. The size distributions show the

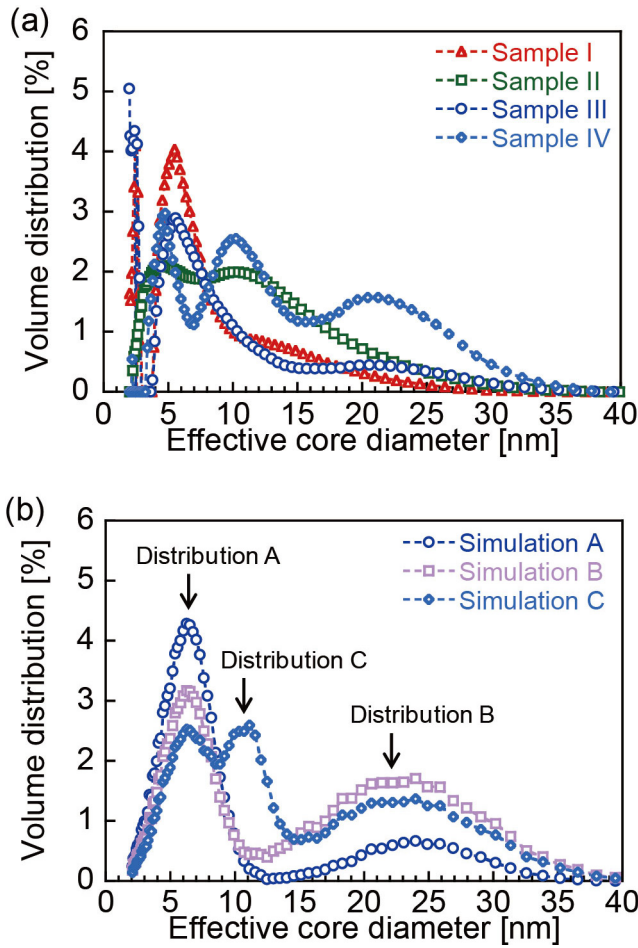


Fig. 1. (a) Volume distribution of the effective core diameters in Samples I, II, III, and IV estimated from DC magnetization measurements. (b) Volume distribution of the effective core diameters for the numerical simulations determined from (a). The effective core particles of 5.5 ± 3 , 20.5 ± 6.5 , and 10 ± 2 nm (mean \pm SD) between the diameters of 2–40 nm were included in distributions A, B, and C.

effective core diameters for each sample, including the single-core, chainlike, and multicore structures, which were observed by a TEM and magnetization measurements in Ref. [9]. The peaks for the small size distributions of 5.4, 7.4, 5.2, and 4.7 nm in samples I, II, III, and IV, respectively, indicated MNPs of the single core structure. The peaks for the multicore structure were confirmed at 20–21 nm in samples III and IV. In addition, the peaks at 10–11 nm in samples II and IV corresponded to the chainlike structure.

Fig. 1 (b) shows the effective core size distribution in the numerical simulation, which is determined from the size distributions of samples III and IV shown in Fig. 1(a). Distributions A, B, and C included the effective core particles with sizes of 5.5 ± 3 , 20.5 ± 6.5 , and 10 ± 2 nm (mean \pm SD) between the diameters of 2–40 nm, which indicated the single-core, multicore, and chainlike structures, respectively. Simulations A and B were the sum of the distributions A and B. Simulation C was the sum of the distributions A, B, and C. The ratios of each distribution in simulations A–C were also determined from the ratios of the distribution in samples III and IV. To evaluate the dependence of the particle structures on the harmonic properties in the same distribution with respect to each structure, distributions A–C were prepared instead of the exact size distribution in Fig. 1(a).

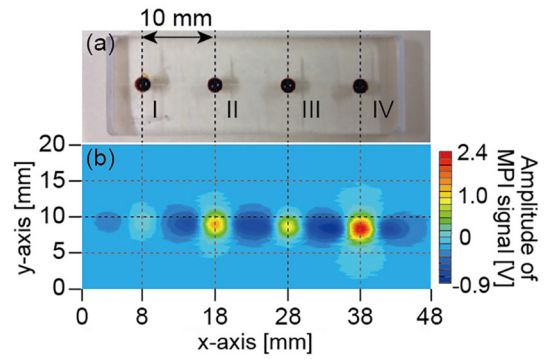


Fig. 2. (a) Measured MNPs in the sample holder and (b) 2D images as the distributions of the MPI signal amplitude in samples I, II, III, and IV. The gradient field is 1 T/m along the x-axis and 2 T/m along the y-axis. The flux density and frequency of the applied AC field are 3.5 mT and 3 kHz, respectively.

3. Results and discussion

3.1. 2D image of MPI and harmonic properties

Fig. 2 shows the 2D images obtained by scanning each sample using the measurement system. The maximal value and the full width at half maximum (FWHM) of the real part of the third harmonic as the MPI signal in Fig. 2 are shown in Fig. 3(a) and (b). These values are dimensionless parameters because they are normalized by the values for sample I. The negative values of the real part of the third harmonic shown in Fig. 2 were derived from the magnetization response to the AC drive field with the DC bias field out of the FFP. When the FFP was located in the position without the samples, the large amplitude of the DC gradient field was applied to the samples. The maximal value of the MPI signal in sample II is higher than those of samples I and III because its core diameter is larger than those of the other two samples. The MPI signal of sample IV is higher than those of the other samples because the MNPs with large magnetization were collected through magnetic separation. Fig. 3(c) shows the third harmonic amplitude (M_3) normalized by fundamental amplitude M_1 , i.e., M_3/M_1 . The value of M_3/M_1 depends on the samples, similar to the FWHM values associated with the nonlinearity of magnetization response to the applied field. When M_3/M_1 increased, the FWHM value decreased with regard to the measured samples (Fig. 3(c)). The high M_3/M_1 and the low FWHM indicates the high resolution for the MPI.

3.2. Numerical simulations in multicore structures with large effective core diameter

3.2.1. Effects of effective anisotropy on harmonic properties

The dependence of M_3/M_1 and M_3 (liquid/solid) on the anisotropy constant is evaluated with respect to the multicore structure shown as distribution B in Fig. 4(a). As the anisotropy constant increases, M_3/M_1 and the ratio of M_3 in the liquid state to that in the solid state, i.e., M_3 (liquid/solid), first decrease and then increase. Fig. 4(b) shows the rotational degree of the easy axis, $\langle \cos \theta \rangle$, where θ is the angle between the directions of the easy axis and applied field. The rotation of the easy axis is delayed from the applied field because of the long Brownian relaxation times of the distributed particles. The range between the maximal and minimal rotational degrees of the easy axis increases with the anisotropy constant. In the case of low anisotropy, the easy axis is steadily oriented in the direction of the applied field because the lowest $\langle \cos \theta \rangle$ is higher than 0.5 in Fig. 4(b).

Fig. 4(c) shows the magnetization curves with effective anisotropy constants of 2 and 3.5 kJ/m³ in Fig. 4(a). The maximal magnetizations in both the solid and liquid states decreased with the increase in the anisotropy constant. In the solid state, the large anisotropy energy

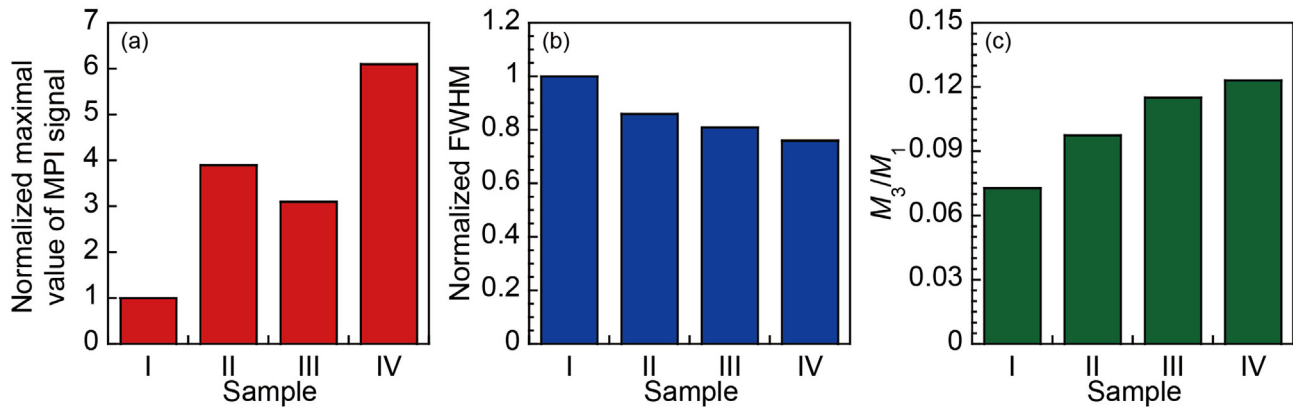


Fig. 3. (a) Maximal values and (b) the full width at half maximum (FWHM) of the real part of the third harmonic as the MPI signals normalized by the values for Sample I with respect to the 2D images shown in Fig. 2. (c) The third harmonic amplitude (M_3) normalized by fundamental amplitude M_1 (M_3/M_1) measured without the gradient field. The flux density and frequency of the applied AC field are 10 mT and 10 kHz, respectively.

barrier inhibited the magnetization. In the liquid state, the magnetization rotation was also inhibited by the anisotropy in spite of the rotation of the easy-axis. It is indicated that the magnetization in the liquid state is easy to orient in the direction of the applied field in the condition of the constant orientation of the easy axis in the direction of the applied field compared to the condition where the easy axis rotates along with the magnetization by large anisotropy [26–28].

3.2.2. Effects of effective core size on harmonic properties

Fig. 5(a) shows the M_3/M_1 and M_3 (liquid/solid) of individual particles with different core diameters in distribution B as multicore particles in the solid and liquid states. The effective anisotropy constant was 2.5 kJ/m³ in Fig. 5. Basically, M_3/M_1 and M_3 (liquid/solid) increase with core diameters owing to the increase in magnetization and anisotropy energy. With respect to the MNPs with core diameters larger than 24 nm, M_3/M_1 decreases with core diameters because the anisotropy energy barrier is too high for the magnetization to overcome. The magnetization curves shown in Fig. 5(b) indicate that the magnetization is gradually changed from the superparamagnetic regime of the small core diameter to the ferromagnetic regime of the large core diameter in the solid state. In the case of multicore particles, it is easier for magnetization to overcome the anisotropy energy barrier compared to the case of single-core and chainlike particles because of large effective core diameter and low effective anisotropy. In particular, the multicore particles with small core diameters indicate the magnetization response based on the Langevin equation as the superparamagnetic regime.

The magnetization curve for the core diameter of 12 nm in the liquid state is marginally changed from that in the solid state because of low anisotropy energy. The rotational degree of the easy axis is small in the core diameter of 12 nm and increases with the increment in diameter (Fig. 5(c)). When the anisotropy energy is low, the easy axis simply orients toward the direction of the applied field and relaxes in the low flux density of the applied field. In addition, with respect to the rotation of the easy axis, the phase delay from the applied field also increases with the increment in the core diameter, because of long Brownian relaxation times in the large hydrodynamic diameters. In particular, $\langle \cos \theta \rangle$ is smaller than 0.5 in the core diameter of 32 nm around the lowest peak values. It is indicated that the easy axis distributes toward the direction perpendicular to the applied field.

3.2.3. Models of magnetization and easy axis responding to magnetic field

To prove the traceability of the easy axis to the magnetization in large core diameters, the time evolutions of the direction of the easy axes with respect to the different core diameters are observed in terms of a randomly extracted single particle (Fig. 6(a–d)). Fig. 6(e) corresponds to the relation between the single particle model and the

rotational degrees. The rotational degree of 0 and 2π showed the same condition. The positive direction of the applied field was shown as the degree of 0 or 2π , and its negative direction was shown as the degree of π . In addition, with respect to the easy axis, the origin symmetry is applied because the potential energy $E = K_u V_M \sin^2(\theta - \varphi) - \mu_0 M_s V_M \cos(\theta)$, which is indicated by the Stoner-Wohlfarth model, is same in the origin symmetry [29]. The angle between the magnetization and the applied field was φ . In Fig. 6(b–d), θ and φ were observed as the rotational degree of the easy axis and the magnetization, respectively.

Fig. 6(f–h) illustrates the distributions of the easy axis and the models of the single particle for each diameter. First, it is indicated that the influence of the thermal disturbance on the magnetization decreases with the increase in core diameter because of the large potential energy. The direction of the easy axis is marginally related to that of the magnetization because of the low anisotropy energy in a small core diameter such as 12 nm (Fig. 6(f)). The easy axis is fully relaxed in the zero field and shows the lowest distribution (Fig. 5(c) and 6(f)). When the anisotropy energy is high owing to a large core diameter such as 32 nm, the easy axis significantly traces the direction of the magnetization rotation (Fig. 6(d)). When the direction of the magnetization is reversed, the easy axis tends to distribute toward the direction perpendicular to the applied field with the rotational degree around $\pi/2$ or $3\pi/2$ as shown in Fig. 6(d, h), which corresponds to the $\langle \cos \theta \rangle$ lower than 0.5 in Fig. 5(c). In the core diameter of 20 nm, the easy axis tends to orient and oscillate around the direction of the applied field (Fig. 6(c)). The easy axis quasi relaxes in the low flux density of the applied field with constant orientation toward the direction of the applied field (Fig. 6(g)). The magnetization has already reversed in the lowest rotational degree of the easy axis in the core diameter of 20 nm because the anisotropy energy is not large enough to bind the magnetization to the easy axis in the low flux density of the applied field (Fig. 5(b), (c), and 6(g)). In addition, it is indicated that the reversal of the easy axis from the rotational degree around π to that around 2π in the duration around 0.05 ms in Fig. 6(c) is due to thermal disturbance, and marginally affects the rotation of the magnetization because of the origin symmetry of the easy axis. When the applied field showed a positive value, the dots of the magnetization and the easy axis were distributed from 0 to $\pi/2$ and from $3\pi/2$ to 2π . This indicates the oscillation of the magnetization and the easy axis around the rotational degree of 0 as the direction of the applied field due to the thermal disturbance.

In terms of the high anisotropy energy, the case of large core diameters is similar to the case of a large anisotropy constant. In Fig. 5(c), the maximal rotational degree of the easy axis increases with the increase in core diameter owing to the large magnetic torque [30]. However, it is constant regardless of the anisotropy constant (Fig. 4(b)).

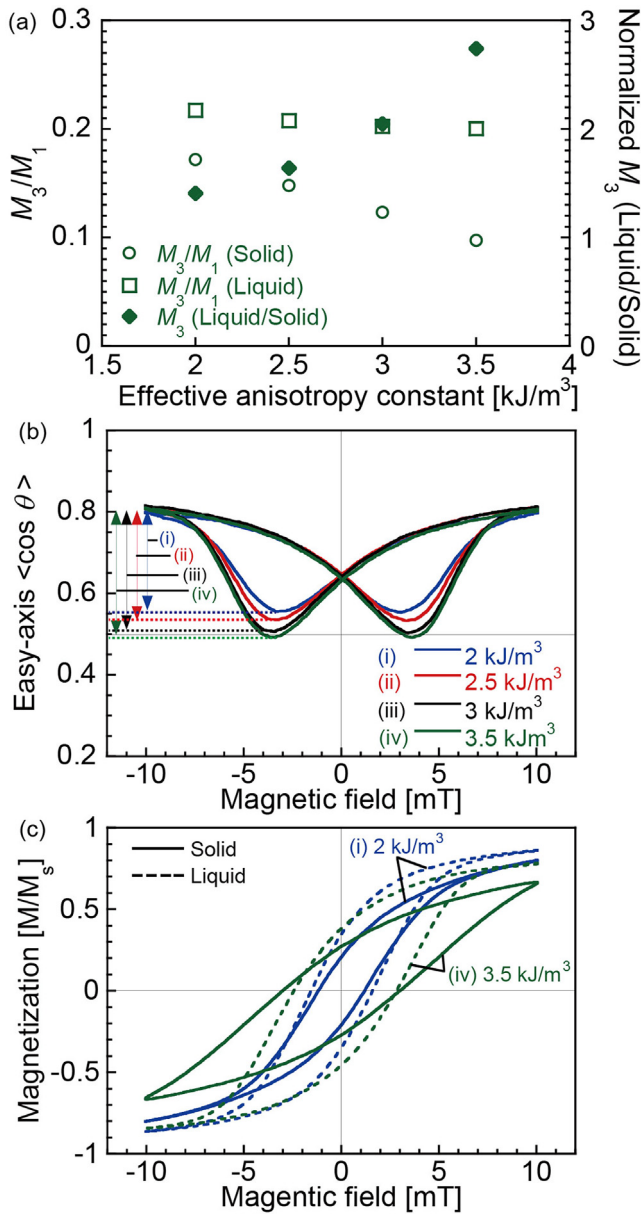


Fig. 4. Dependence of (a) the third harmonic amplitude (M_3) normalized by the fundamental amplitude M_1 , M_3/M_1 , the ratio of M_3 in the liquid state to that in the solid state, M_3 (liquid/solid), and (b) the rotational degree of the easy axis, $\langle \cos \theta \rangle$, on the effective anisotropy constant for multicore particles. θ is the angle between the easy axis and applied field. The distribution of the particle diameters is the same as distribution B. (c) AC magnetization curves in the anisotropy constants of 2 and 3.5 kJ/m^3 are also shown. The flux density and frequency of the AC field are 10 mT and 10 kHz, respectively.

Thus, the traceability of the easy axis to the magnetization is determined by the anisotropy energy associated with both core diameter and anisotropy constant. The maximal rotational degree of the easy axis is influenced by the core diameter affecting the magnetic torque. The ratios of the Néel relaxation time τ_N to the Brownian relaxation time τ_B (τ_N/τ_B) were 0.0030, 0.0026, and 0.79 for the core diameters of 12, 20, and 32 nm, respectively. At the intercept point for the Néel and Brownian relaxation times, the core diameter was 32.3 nm in 2.5 kJ/m^3 of the anisotropy constant. Even though the relation of $\tau_B \gg \tau_N$ was confirmed in 12 and 20 nm, the traceability of the easy axis to the magnetization was enhanced in 20 nm. It was found that the traceability of the easy axis is dependent on the anisotropy energy rather than the ratio of the relaxation time τ_N/τ_B , despite the large value of τ_N/τ_B .

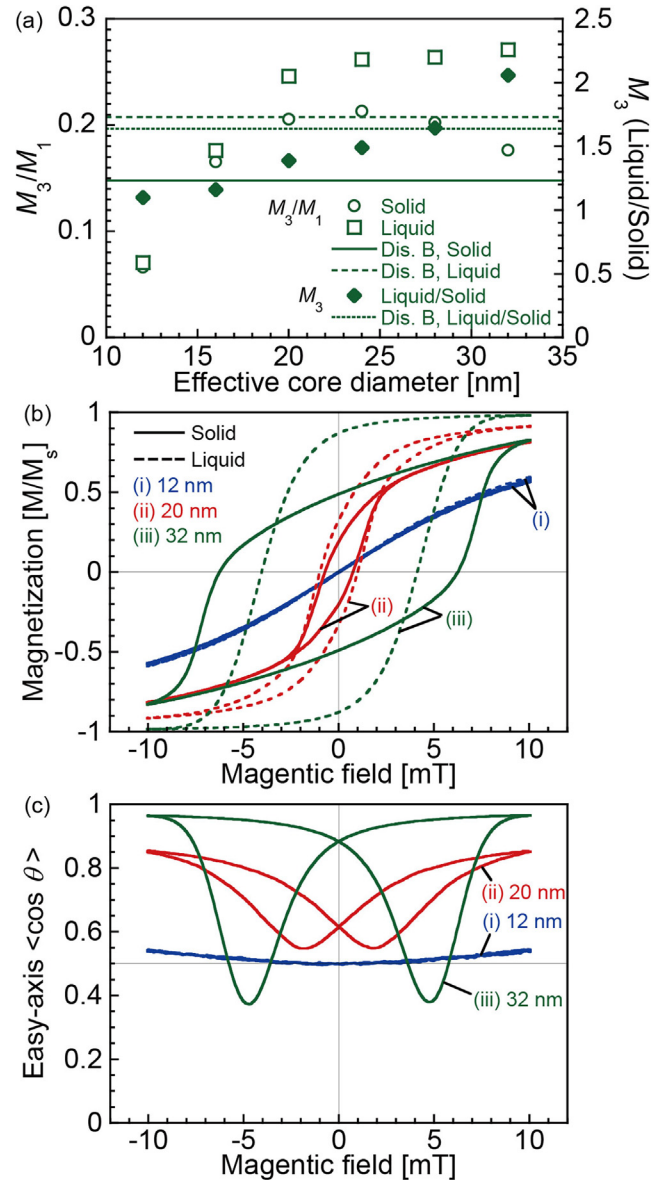


Fig. 5. Dependence of (a) the third harmonic amplitude (M_3) normalized by the fundamental amplitude M_1 , M_3/M_1 , the ratio of M_3 in the liquid state to that in the solid state, M_3 (liquid/solid), on the effective core diameters including distribution B as multicore particles. (b) The rotational degree of the easy axis, $\langle \cos \theta \rangle$, and (c) AC magnetization curves for the core diameters of 12, 20, and 32 nm were observed. θ is the angle between the easy axis and applied field. The flux density and frequency of the AC field are 10 mT and 10 kHz, respectively.

τ_B in 32 nm.

3.3. Effective magnetism in characteristic structures of MNPs determined from experiments and numerical simulations

Fig. 7(a) and (b) show the AC magnetization curves obtained for samples III and IV and for simulations A, B, and C, respectively, in the solid and liquid states. Samples III and IV were chosen as the experimental results for the comparison with the results of the numerical simulation because sample IV was the sample magnetically separated from sample III. The effects of the core diameter and anisotropy on the nonlinear response of the magnetization is clearly observed in samples III and IV. The harmonic properties dependent on the particle structures were confirmed in the range of 1–100 kHz, and their frequency

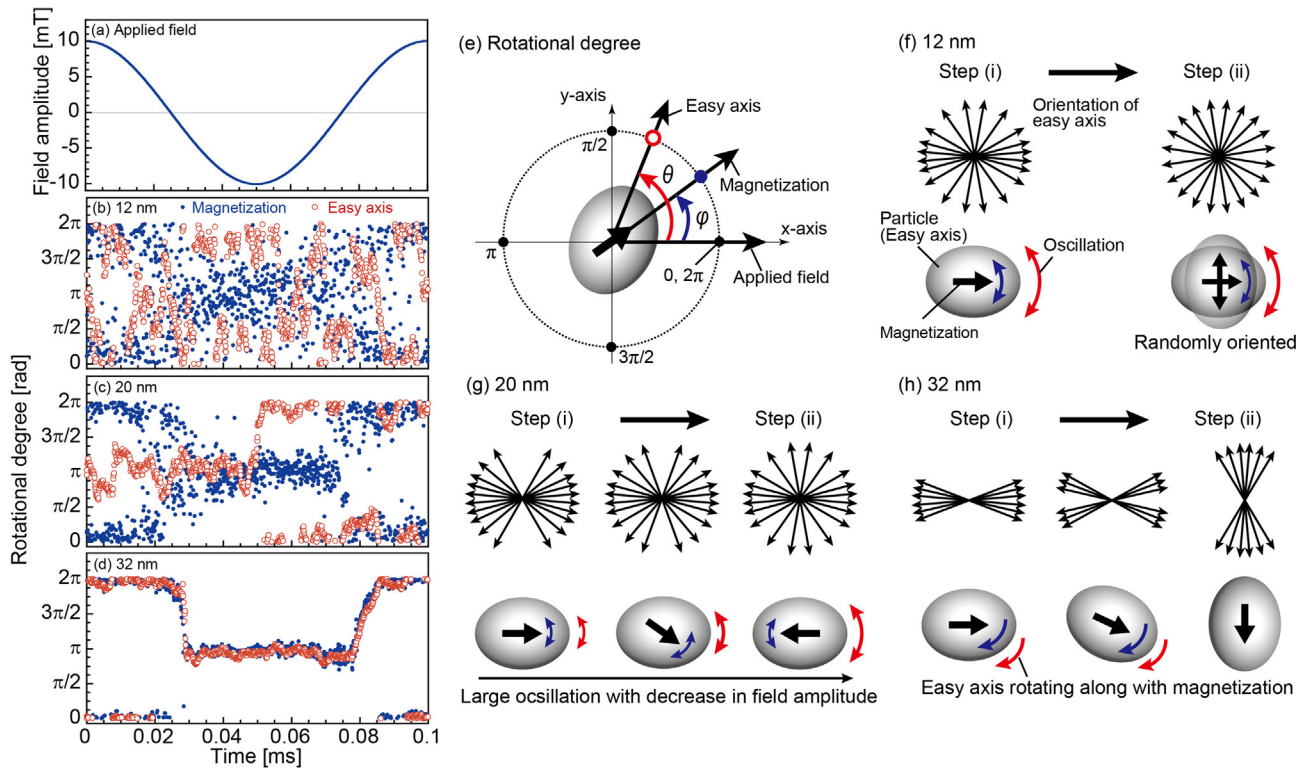


Fig. 6. Time evolution of (a) the flux density of applied field, and the magnetization and easy axis of a randomly extracted single particle for the core diameters of (b) 12 nm, (c) 20 nm, and (d) 32 nm. The solid and open dots show the magnetization and easy axis, respectively. The frequency of the applied field was 10 kHz. (e) relation between the single particle model and the rotational degrees. The rotational degrees of 0 (positive direction) and π (negative direction). Distributions of the easy axis and the single-particle models for the core diameters of (f) 12 nm, (g) 20 nm, and (h) 32 nm in the maximal flux density of the applied field (Step (i)) and the lowest distribution of the easy axis in Fig. 5(c) (Step (ii)). The arrows distributed in a circular pattern show the orientation of the easy axis as the model of the total distribution of the easy axis in Fig. 5(c).

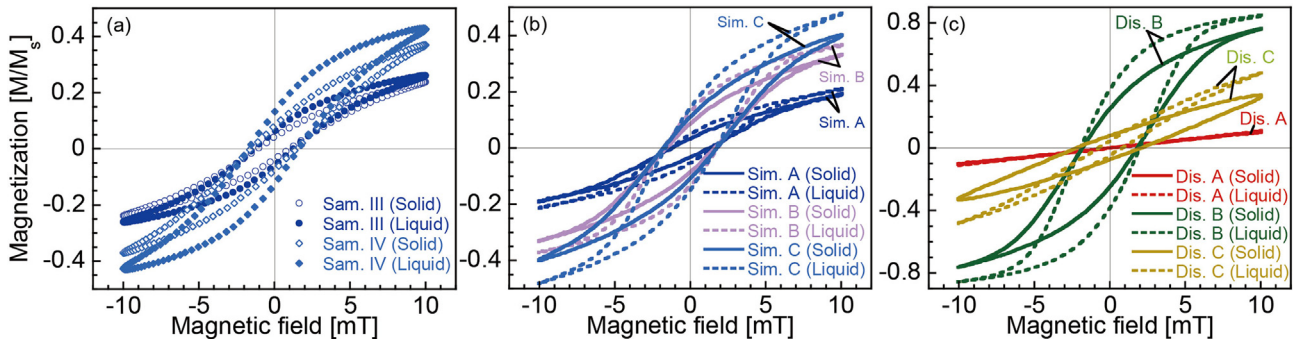


Fig. 7. AC magnetization curves of (a) samples (sam.) III and IV, (b) simulations (sim.) A, B, and C, and (c) distributions (dis.) A, B, and C in the solid and liquid states. The flux density and frequency of the applied AC field are 10 mT and 10 kHz, respectively, in all cases. The measured results are shown in (a). The results in (b) and (c) are numerically simulated.

dependence has been discussed in our previous research [9]. The amplitude of the third harmonic decreased with the increase in frequency with the phase delay from the applied field.

The AC magnetization curves in distributions A, B, and C are shown in Fig. 7(c). In distributions A and C as the single-core and chainlike structures, the effective anisotropy constant was 16 kJ/m³. With respect to the single-core particle of the small core diameter, the surface anisotropy was large [31]. In the chainlike structure, the dipole interaction enhances the uniaxial anisotropy as the shape effect [32,33]. The effective anisotropy constant was determined as 2.5 kJ/m³ in distribution B. M_3 and M_3/M_1 were evaluated using the AC magnetization signals, and they are shown in Table 1. The M_3 and M_3/M_1 of simulation B are larger than those of simulation A because of the high distribution of the multicore structures in simulation B. However, M_3 (liquid/solid) in

simulations A and B is similar to that of distribution B. The influence of the M_3 derived from multicore particles on the total M_3 of the sample is dominant in comparison with the single-core particles. Even though the M_3 of simulation C is larger than that of simulation B, the M_3/M_1 of simulation C is smaller than that of simulation B. The M_3 (liquid/solid) of distribution C is significantly larger than that of distribution B. Both M_3/M_1 and M_3 (liquid/solid) in sample IV were larger than those in sample III. The ratio of the multicore and chainlike structures in sample IV was found to increase compared to sample III, which is characterized by the peaks in 10–11 nm and 20–21 nm ranges of the size distribution in Fig. 1(a). In particular, the steep slope of the magnetization curve associated with the nonlinear response of the magnetization was shown by M_3/M_1 .

In the superparamagnetic regime, the coercivity in the liquid state

Table 1

Third harmonic M_3 in solid and liquid states, the ratio of M_3 in the liquid state to that in the solid state, M_3 (liquid/solid), and M_3 normalized by fundamental amplitude M_1 (M_3/M_1) in solid and liquid states for (a) samples (sam.) III and IV, (b) simulations (sim.) A, B, and C, and (c) distributions (dis.) A, B, and C. The flux density and frequency of the AC field are 10 mT and 10 kHz, respectively, in all cases.

	Sam. III	Sam. IV	Sim. A	Sim. B	Sim. C	Dis. A	Dis. B	Dis. C
M_3 (Solid)	0.0229	0.0334	0.0178	0.0447	0.0471	0.00103	0.128	0.00925
M_3 (Liquid)	0.0330	0.0589	0.0286	0.0729	0.0807	0.000541	0.209	0.0268
M_3 (Liquid/Solid)	1.44	1.76	1.61	1.63	1.71	0.523	1.64	2.90
M_3/M_1 (Solid)	0.0890	0.0838	0.0874	0.122	0.108	0.0104	0.148	0.0270
M_3/M_1 (Liquid)	0.115	0.123	0.123	0.173	0.149	0.00491	0.208	0.0531

was larger than that in the solid state because the Brownian relaxation occurred with the Néel relaxation in the liquid state, and the phase delay of the magnetization increased in the liquid state. On the other hand, the coercivity decreased in the ferromagnetic particles except for the effect of the magnetic relaxation because the easy axis rotated along with the magnetization and the anisotropy energy barrier declined in the liquid state. The anisotropy of the chainlike structure binds the magnetization to the easy axis and induces the ferromagnetic regime in the solid state. In distribution C, the coercivity in the liquid state was smaller than that in the solid state. Distribution C showed the strong ferromagnetic regime, which resulted in the high M_3 (liquid/solid) value. The magnetization in the solid state was inhibited by the high anisotropy energy barrier in comparison with that in the liquid state. The effective transition from the ferromagnetic regime in the solid state to the superparamagnetic regime in the liquid state was also observed as the lower imaginary part of susceptibility in the liquid state than that in the solid state [34]. In terms of the chainlike structure, when the easy axis is rotatable in the liquid state, high anisotropy promotes the rotation of the easy axis, which results in the nonlinear response of the magnetization [17,31].

As shown in Fig. 4(c), as the coercivity in the liquid state is smaller than that in the solid state with an effective anisotropy constant of 3.5 kJ/m³, which is lower than the bulk magnetocrystalline anisotropy constant of γ -Fe₂O₃ (4.6 kJ/m³) [34]. On the other hand, the AC magnetization curves in samples III and IV including the multicore structure, the coercivity in the liquid state was slightly larger than that in the solid state due to the Brownian relaxation. With respect to the multicore structure, the superparamagnetic regime was dominant, and the effective anisotropy constant lower than 2.5 kJ/m³ in the numerical simulation in Fig. 7 was applicable. In contrast to the demagnetizing effect of the dipole interaction in the short interparticle distance [35,36], the effective magnetization in the multicore structure is enhanced compared to the single-core particle. In the multicore structure, the role of the exchange interaction is dominant, which is associated with the superparamagnetic regime [37]. It is indicated that the isotropic behavior in the multicore structure was due to the magnetic coupling among the randomly aggregated core particles.

4. Conclusions

We evaluated the dependences of the effective size and the effective anisotropy, influenced by the particle structures, on the magnetization harmonic. The measurements of the MPI signal indicated that M_3 and M_3/M_1 were applicable as the evaluation indexes of the harmonic amplitude and FWHM, respectively. A large core diameter induced large M_3 and M_3/M_1 , and large anisotropy increased the ratio of M_3 in the liquid state to that in the solid state. In contrast, when the anisotropy was small with respect to the MNPs with a large core diameter, M_3 and M_3/M_1 were large in the solid and liquid states. Consequently, it was revealed that the multicore structure induced the nonlinear response of the magnetization as the steep magnetization curve because of the large effective core diameter and small effective anisotropy. The anisotropy of the chainlike structure was large owing to unidirectional dipole interaction. Thus, the structure with a large core diameter and

small anisotropy, such as the multicore structure, played a key role in the large amplitude of the MPI signal and the high resolution, which is also satisfied by the single-core structure with large core diameter, isotropic shape, and small magnetocrystalline anisotropy. On the contrary, the difference of the MPI signal between the states of MNPs, for instance, in tumors, organs, and blood, whose viscosity is changes with human health, was enhanced by the chainlike structure due to the large anisotropy. However, because the harmonic amplitude in the chainlike structure is lower than that of the multicore structure, it is necessary that the ratio between the MNPs of the chainlike and other structures was adjusted to keep the resolution high enough for detecting the MPI signal.

Acknowledgment

This work was partially supported by the JSPS KAKENHI Grant Numbers 15H05764, 17H03275, and 17K14693.

References

- [1] B. Gleich, J. Weizenecker, Tomographic imaging using the nonlinear response of magnetic particles, *Nature* 435 (2005) 1214.
- [2] J. Weizenecker, B. Gleich, J. Rahmer, H. Dahnke, J. Borgert, Three-dimensional real-time in vivo magnetic particle imaging, *Phys. Med. Biol.* 54 (2009) L1.
- [3] Y.Y. Elaine, P. Chandrasekharan, R. Berzon, Z.W. Tay, X.Y. Zhou, A.P. Khandhar, R.M. Ferguson, S.J. Kemp, B. Zheng, P.W. Goodwill, M.F. Wendland, K.M. Krishnan, S. Behr, J. Carter, S.M. Conolly, Magnetic particle imaging for highly sensitive, quantitative, and safe in vivo gut bleed detection in a murine model, *ACS Nano* 11 (2017) 12067.
- [4] H. Arami, E. Teeman, A. Troksa, H. Bradshaw, K. Saatchi, A. Tomitaka, S.S. Gambhir, U.O. Häfeli, D. Liggitt, K.M. Krishnan, Tomographic magnetic particle imaging of cancer targeted nanoparticles, *Nanoscale* 9 (2017) 18723.
- [5] E.Y. Yu, M. Bishop, B. Zheng, R.M. Ferguson, A.P. Khandhar, S.J. Kemp, K.M. Krishnan, P.W. Goodwill, S.M. Conolly, Magnetic particle imaging: a novel in vivo imaging platform for cancer detection, *Nano Lett.* 17 (2017) 1648–1654.
- [6] B. Zheng, M.P. von See, E. Yu, B. Gunel, K. Lu, T. Vazin, D.V. Schaffer, P.W. Goodwill, S.M. Conolly, Quantitative magnetic particle imaging monitors the transplantation, biodistribution, and clearance of stem cells in vivo, *Theranostics* 6 (2016) 291–301.
- [7] J.E. Lemaster, F. Chen, T. Kim, A. Hariri, J.V. Jokerst, Development of a trimodal contrast agent for acoustic and magnetic particle imaging of stem cells, *ACS Appl. Nano Mater.* 1 (2018) 1321–1331.
- [8] P. Wang, P.W. Goodwill, P. Pandit, J. Gaudet, A. Ross, J. Wang, E. Yu, D.W. Hensley, T.C. Doyle, C.H. Contag, S. Conolly, A. Moore, Magnetic particle imaging of islet transplantation in the liver and under the kidney capsule in mouse models *Quant. Imag. Med. Surg.* 8 (2018) 144 122.
- [9] S. Ota, R. Takeda, T. Yamada, I. Kato, S. Nohara, Y. Takemura, Effect of particle size and structure on harmonic intensity of blood-pooling multi-core magnetic nanoparticles for magnetic particle imaging, *Int. J. Magn. Part. Imag.* 3 (2017) 1703003.
- [10] R.M. Ferguson, K.R. Minard, A.P. Khandhar, K.M. Krishnan, Optimization of nanoparticle core size for magnetic particle imaging, *Med. Phys.* 38 (2011) 3.
- [11] A. Tomitaka, R.M. Ferguson, A.P. Khandhar, S.J. Kemp, S. Ota, K. Nakamura, Y. Takemura, K.M. Krishnan, Variation of magnetic particle imaging tracer performance with amplitude and frequency of the applied magnetic field, *IEEE Trans. Magn.* 51 (2015) 2.
- [12] Z.W. Tay, D.W. Hensley, E.C. Vreeland, B. Zheng, S.M. Conolly, The relaxation wall: experimental limits to improving MPI spatial resolution by increasing nanoparticle core size, *Biomed. Phys. Eng. Express* 3 (2017) 035003.
- [13] D. Eberbeck, C.L. Dennis, N.F. Huls, K.L. Krycka, C. Grüttnner, F. Westphal, Multicore Magnetic Nanoparticles for Magnetic Particle Imaging, *IEEE Trans. Magn.* 49 (2013) 269.
- [14] T. Yoshida, N.B. Othman, K. Enpuku, Characterization of magnetically fractionated magnetic nanoparticles for magnetic particle imaging, *J. Appl. Phys.* 114 (2013) 173908.

- [15] S. Dutz, J. Clement, D. Eberbeck, T. Gelbrich, R. Hergt, R. Müller, J. Wotschadlo, M. Zeisberger, Ferrofluids of magnetic multicore nanoparticles for biomedical applications, *J. Magn. Magn. Mater.* 321 (2009) 1501–1504.
- [16] T. Yoshida, S. Bai, A. Hirokawa, K. Tanabe, K. Enpuku, Effect of viscosity on harmonic signals from magnetic fluid, *J. Magn. Magn. Mater.* 380 (2015) 105–110.
- [17] S. Ota, R. Kitaguchi, R. Takeda, T. Yamada, Y. Takemura, Rotation of magnetization derived from Brownian relaxation in magnetic fluids of different viscosity evaluated by dynamic hysteresis measurements over a wide frequency range, *Nanomaterials* 6 (2016) 170.
- [18] D. Cabrera, A. Lak, T. Yoshida, M.E. Materia, D. Ortega, F. Ludwig, P. Guardia, A. Sathya, T. Pellegrino, F.J. Teran, Unraveling viscosity effects on the hysteresis losses of magnetic nanocubes, *Nanoscale* 9 (2017) 5094–5101.
- [19] S.B. Trisnanto, S. Ota, Y. Takemura, Two-step relaxation process of colloidal magnetic nanoclusters under pulsed fields, *Appl. Phys. Express* 11 (2018) 075001.
- [20] S. Ota, Y. Takemura, Evaluation of easy-axis dynamics in a magnetic fluid by measurement and analysis of the magnetization curve in an alternating magnetic field, *Appl. Phys. Express* 10 (2017) 085001.
- [21] N. Nitta, K. Tsuchiya, A. Sonoda, S. Ota, N. Ushio, M. Takahashi, K. Murata, S. Nohara, Negatively charged superparamagnetic iron oxide nanoparticles: a new blood-pooling magnetic resonance contrast agent, *Jpn. J. Radiol.* 30 (2012) 832–839.
- [22] W.T. Coffey, Y.P. Kalmykov, Internal effects in the complex magnetic susceptibility of a ferrofluid in the presence of a dc bias field, *J. Magn. Magn. Mater.* 164 (1996) 133.
- [23] K.D. Usadel, Dynamics of magnetic nanoparticles in a viscous fluid driven by rotating magnetic fields, *Phys. Rev. B* 95 (2017) 104430.
- [24] W.T. Coffey, Y.P. Kalmykov, *The Langevin Equation: With Applications to Stochastic Problems in Physics, Chemistry and Electrical Engineering*, 3rd ed., World Scientific, Singapore, 2012, pp. 126–130.
- [25] T. Sasayama, T. Yoshida, M.M. Saari, K. Enpuku, Comparison of volume distribution of magnetic nanoparticles obtained from M-H curve with a mixture of log-normal distributions, *J. Appl. Phys.* 117 (2015) 17D155.
- [26] S.A. Shah, D.B. Reeves, R.M. Ferguson, J.B. Weaver, K.M. Krishnan, Mixed Brownian alignment and Néel rotations in superparamagnetic iron oxide nanoparticle suspensions driven by an ac field, *Phys. Rev. B* 92 (2015) 094438.
- [27] T. Yoshida, Y. Matsugi, N. Tsujimura, T. Sasayama, K. Enpuku, T. Viereck, M. Schilling, F. Ludwig, Effect of alignment of easy axes on dynamic magnetization of immobilized magnetic nanoparticles, *J. Magn. Magn. Mater.* 427 (2017) 162–167.
- [28] R. Takeda, S. Ota, T. Yamada, Y. Takemura, Dynamic hysteresis measurement of magnetic nanoparticles with aligned easy axes, *J. Magn. Soc. Jpn.* 42 (2018) 55–61.
- [29] E.C. Stoner, E.P. Wohlfarth, A mechanism of magnetic hysteresis in heterogeneous alloys, *Philos. Trans. R. Soc. London, Ser. A* 240 (1948) 599.
- [30] P. Dutta, S. Pal, M.S. Seehra, N. Shah, G.P. Huffman, Size dependence of magnetic parameters and surface disorder in magnetite nanoparticles, *J. Appl. Phys.* 105 (2009) 07B501.
- [31] J. Carrey, N. Hallali, Torque undergone by assemblies of single-domain magnetic nanoparticles submitted to a rotating magnetic field, *Phys. Rev. B* 94 (2016) 184420.
- [32] L.C. Branquinho, M.S. Carrião, A.S. Costa, N. Zufelato, M.H. Sousa, R. Miotto, R. Ivkov, A.F. Bakuzis, Effect of magnetic dipolar interactions on nanoparticle heating efficiency: implications for cancer hyperthermia, *Sci. Rep.* 3 (2013) 2887.
- [33] D. Serantes, K. Simeonidis, M. Angelakeris, O. Chubykalo-Fesenko, M. Marciello, M. del, P. Morales, D. Baldomir, C. Martinez-Boubeta, Multiplying magnetic hyperthermia response by nanoparticle assembling, *J. Phys. Chem. C* 118 (2014) 5927–5934.
- [34] R. Hergt, R. Hiergeist, I. Hilger, W.A. Kaiser, Y. Lapatnikov, S. Margel, U. Richter, Maghemite nanoparticles with very high AC-losses for application in RF-magnetic hyperthermia, *J. Magn. Magn. Mater.* 270 (2004) 345–357.
- [35] J.G. Ovejero, D. Cabrera, J. Carrey, T. Valdivielso, G. Salas, F.J. Teran, Effects of inter- and intra-aggregate magnetic dipolar interactions on the magnetic heating efficiency of iron oxide nanoparticles, *Phys. Chem. Chem. Phys.* 18 (2016) 10954–10963.
- [36] P. Ilg, Equilibrium magnetization and magnetization relaxation of multicore magnetic nanoparticles, *Phys. Rev. B* 95 (2017) 214427.
- [37] L. Lartigue, P. Hugounenq, D. Alloyeau, S.P. Clarke, M. Lévy, J.-C. Bacri, R. Bazzi, D.F. Brougham, C. Wilhelm, F. Gazeau, Cooperative organization in iron oxide multi-core nanoparticles potentiates their efficiency as heating mediators and MRI contrast agents, *ACS Nano* 6 (2012) 10935–10949.